

Heat Transfer Characteristics Based on Microlayer Structure in Nucleate Pool Boiling for Water and Ethanol

Yoshio Utaka, Yuki Kashiwabara, Michio Ozaki and Zhihao Chen

* Corresponding author. Tel/Fax: +81 45 339 3909.

E-mail: utaka@ynu.ac.jp

1. Introduction

The boiling phenomenon, which involves heat transfer factors, such as high heat transfer coefficient, high critical heat flux, and utilization of both liquid and vapor phases, is widely used in numerous industries. Although a number of studies have examined the boiling phenomena, unknown quantitative factors affect the heat transfer mechanisms of boiling due to complex physicochemical factors, such as bubble nucleation, growth, and fluid motions, and phase changes at the liquid-vapor interface.

The heat transfer mechanisms of nucleate boiling have been classified into two categories of convective heat transfer and latent heat transfer. The convective heat transfer mechanism is based on diffusion of the thermal boundary layer by bubble motion and sensible heat transport, whereas the latent heat transfer mechanism involves sensible heat stored in the superheated liquid layer being converted into bubble growth and vaporization of the microlayer that forms between a growing bubble and the heat transfer surface. Although the heat transfer mechanism of nucleate boiling has been investigated in terms of these proposed mechanisms, there has not been sufficient quantitative investigation. The heat transfer characteristics of microlayer evaporation, in which a large amount of heat transport results from latent heat of evaporation, is especially important. Therefore, clarification of the microlayer structure is fundamental to understanding the boiling process.

Measurement of the microlayer can be classified into two methods. One involves prediction of the microlayer thickness from the unsteady temperature variation of the heat transfer surface. Moore and Mesler [1] first experimentally demonstrated the formation of a microlayer formed under boiling water bubbles. Cooper and Lloyd [2] measured the microlayer for various organic liquids. Yabuki and Nakabeppu [3] performed high precision measurements of water using microelectromechanical system (MEMS) sensors. The other type of method involves measurement of the microlayer thickness using optical interferometry. This technique enables direct measurement of the microlayer thickness. Mercury arc lamps were used as light sources in early studies, such as those reported by Sharp [4] who confirmed the presence of a microlayer and measured its thickness for water, and by Jawurek [5] for ethanol. Furthermore, Voutsinos and Judd [6] measured the microlayer thickness in dichloromethane using a laser light source. Koffman and Plesset [7] measured microlayer thickness distributions for subcooled water and ethanol with high-speed photography. Gao et al. [8] recently adopted a similar interferometric method and measured the microlayer thickness for ethanol.

The structure of the microlayer and its effect on heat transfer are understood to a lesser extent, because special measurement devices are often required to investigate the microlayer characteristics for the complex behavior of liquids and vapors during boiling phenomena. Measurements have been mostly performed for only water and several organic liquids; therefore, it is important to systematically investigate the characteristics of the microlayer using various methods, liquids, and conditions.

The previous study of Utaka et al. [9] was advanced to determine the distribution of initial microlayer thickness for water and ethanol using a unique laser extinction method and by developing a method for

initial microlayer thickness determination that combines modeling and numerical calculations for a boiling system with analysis of the microlayer behavior recorded with a high-speed camera [10]. The initial microlayer thickness was found to increase linearly with distance from the bubble site and the measurement results were consistent with those reported by different researchers.

The objective of the present study is to elucidate the contribution of evaporation from the microlayer on pool nucleate boiling heat transfer of the isolated bubble region for water and ethanol through derivation of the microlayer characteristics from previously reported measurement results [9] and simultaneous imaging of vapor bubble inception and growth.

Nomenclature

f	period of bubble formation cycle (ms)
h_i	interfacial heat transfer coefficient due to interphase mass transfer
k_l	thermal conductivity of liquid (W/(m K))
L	latent heat of vaporization (J/kg)
q	heat flux (W/m ²)
q_1	heat flux at backside of heat transfer plate (W/m ²)
q_2	heat flux at heat transfer surface under bulk liquid phase (W/m ²)
q_3	heat flux at heat transfer surface under microlayer (W/m ²)
Q_{ML}	heat transfer rate through the microlayer to the vapor bubble (J)
r	radial axis (distance from origin at bubble inception site) (mm)
R	gas constant (J/(kg K))
R_{Bmax}	maximum bubble radius of horizontal direction (mm)
R_{dry}	radius of the dryout region (mm)
R_M	microlayer radius on heat transfer surface (mm)
R_{Mmax}	maximum microlayer radius (mm)
t	time (ms)
t_B	elapsed time from bubble inception (ms)
t_{Bd}	elapsed time from bubble inception to completion of bubble departure (ms)
t_g	time prior to initial microlayer formation at r (s)
t_{Mmax}	time elapsed before maximum radius of microlayer R_{Mmax} (ms)
t_{Md}	time elapsed before commencement of bubble departure (ms)
T	temperature (K)
T_{sat}	saturation temperature (K)
T_w	temperature of heat transfer plate (K)
V_B	bubble volume (m ³)
V_{ML}	vapor volume from microlayer evaporation (mm ³)

z	axis perpendicular to heat transfer plate (origin at heat transfer surface) (mm)
α	thermal diffusivity (m ² /s)
δ	microlayer thickness (μm)
δ_0	initial microlayer thickness (μm)
δ_{max}	initial microlayer thickness at R_{Mmax} (μm)
δ_{T}	thickness of superheated layer (mm)
Δt	time step for calculation (ms)
Δt_{Me}	duration of microlayer presence (ms)
ΔT	superheat of the heat transfer surface (K)
ΔT_i	surface superheat temperature at bubble inception (K)
ρ_v	vapor density (kg/m ³)
ρ_l	liquid density (kg/m ³)
σ	evaporation coefficient (–)

2. Summary of previous study

A previous study by Utaka et al. [10] reported measurements of the microlayer structures for water and ethanol under saturated condition using the laser extinction method with a laser emission apparatus and an optical fiber with a core diameter of 94 μm in a thin metal tube located at the head of the growing bubble in the bulk liquid, as shown in Fig. 1. This special device was employed to obtain measurements without contact by removing the bulk liquid between the optical fiber and the microlayer, where the gas blown from the thin tube coalesced with the growing vapor bubble as it developed. The laser extinction method was combined with the special device, which consists of a boiling system of water and ethanol at atmospheric pressure and a system to measure the transmission ratio of laser light. A 2 mm thick quartz glass heat transfer plate and nitrogen gas as a heating medium were used to realize stable transmission of the laser beam to the detector. Figures 2 and 3 show the key results of the previous report [10] for water and ethanol, respectively, including the variation in initial microlayer thickness δ_0 (μm) with measurement position r (mm). Here, the initial microlayer thickness δ_0 is defined as the thickness when the bubble forefront reaches r and the microlayer is formed. The extrapolation was applied to determine δ_0 and surface superheat at bubble inception ΔT_i simultaneously by iteration until agreement was obtained between the measured and calculated variations in the microlayer thickness because there was short duration without data at the beginning of microlayer formation. Heat flux had little effect on the microlayer thickness within the range of measurement. The results clarified that δ_0 increased with the distance from the bubble inception site. The relation between the distance from the bubble inception site and the microlayer thickness are expressed by Eqs. (1) and (2) for water and ethanol, respectively. The dotted lines in the figures indicate the error ranges in the measurements.

$$\delta_0 = 4.46 \times r \quad (1)$$

$$\delta_0 = 10.2 \times r \quad (2)$$

The measurement results obtained by Utaka et al. [10] were consistent with those reported by Koffman and Plesset [7] for water and ethanol, by Yabuki and Nakabeppu [3] for water, and by Gao et al. [8] for ethanol.

3. Basic characteristics and correlations concerning the microlayer in nucleate pool boiling

A schematic diagram of the variation in growth for the vapor bubble and microlayer is shown in Fig. 4, which also defines the dominant physical parameters. A vapor bubble is generated, grows and departs at the inception site, while a microlayer with a radius that increases on the heat transfer surface is formed. The vapor bubble subsequently departs from the surface due to the forces of buoyancy and flow inertia. During the departure process, the radius of the microlayer decreases, the heat transfer surface becomes covered with bulk liquid, and the area of the microlayer disappears. The bubble cycle, in which the superheat of the heating surface recovers during the waiting period and a vapor bubble forms, is then repeated. Although the velocity of bubble growth was different, the qualitative trend in the variation of microlayer radius R_M from vapor generation to bubble departure was analogous. Here, the elapsed time from bubble inception is denoted as t_B and t_{Mmax} is the elapsed time before the appearance of the maximum radius of the microlayer. The elapsed time before completion of bubble departure, the period until the formation of microlayer at r , and the duration of the microlayer at r are t_{Bd} , t_g and ΔT_{Me} , respectively. Each radius and period of time was measured from images acquired simultaneously with the microlayer measurement.

The measured characteristic quantities that determine the features of nucleate boiling are discussed next. Figure 5 shows the variation in growth rate of microlayer radii R_M , which indicates the growth area of the microlayer for water and ethanol as a function of the time elapsed from bubble formation t_B . Only a slight dependence on heat flux was observed, whereas the duration of the microlayer increased with the microlayer radius. The size of the microlayer increased abruptly during the interval of 5-10 ms and reached a maximum, after which it diminished and disappeared during the bubble departure process. After the maximum was reached, the rate of decrease in the microlayer radius was gradual compared to the rate of radius increase.

Figure 6 shows the variation in the time elapsed before completion of bubble departure t_{Bd} , with the maximum radius of the microlayer R_{Mmax} (mm), for water and ethanol. The value of t_{Bd} (ms) increased with R_{Mmax} for each test liquid. The relationships between R_{Mmax} and t_{Bd} for water and ethanol are not quantitatively similar, but indicate a similar tendency for each other. The respective relations are expressed by Eqs. (3) and (4):

$$t_{Bd} = 4.94 \times R_{Mmax} + 6.92 \quad (3)$$

$$t_{Bd} = 5.07 \times R_{Mmax} + 9.78 \quad (4)$$

Furthermore, from Eqs. (1) and (2), the respective relationships between the initial microlayer thickness δ_{\max} (μm) at $R_M = R_{M\max}$ (mm) for water and ethanol can be expressed as:

$$\delta_{\max} = 4.46 \times R_{M\max} \quad (5)$$

$$\delta_{\max} = 10.2 \times R_{M\max} \quad (6)$$

The duration of the microlayer Δt_{Me} , with respect to the distance r is shown in Fig. 7. The duration of the microlayer is widely variable, even at the same distance, and a fixed relation is not easily determined, but the trends of change for water and ethanol are similar. The value of Δt_{Me} decreases with increase in r .

Figure 5 shows that the qualitative trends in the variation of the microlayer radii from bubble formation to departure are similar both for water and ethanol. Therefore, it is possible to obtain systematic correlations among the physical factors concerning bubble and microlayer variation by normalization of the microlayer radius and the bubble growth time. Figure 8 shows the results where the variations in microlayer radii R_M and t_B , from bubble formation to departure were normalized using $R_{M\max}$ and t_{Bd} , respectively. The non-dimensional bubble growth curves show uniform variation and confirm that the microlayer radii for water and ethanol grow in a similar manner. Thus, a better correlation was obtained by normalization.

The relation between the local position and duration of the microlayer shown in Fig. 7 was converted to a non-dimensional form using $R_{M\max}$ and t_{Bd} , as shown in Fig. 9. The cohesiveness of the data is promoted by normalization and indicates that water and ethanol have almost equal relations. The relation for both materials in bulk can be expressed as:

$$\frac{\Delta t_{\text{Me}}}{t_{\text{Bd}}} = -0.662 \times \frac{r}{R_{M\max}} + 0.941. \quad (7)$$

The relations between the initial microlayer thickness and the local position (Figs. 2 and 3) were normalized similarly using δ_{\max} and $R_{M\max}$ with respect to the heat flux q , as shown in Fig. 10. There is no dependency on q in this experimental range; therefore, the non-dimensional microlayer thickness can be expressed uniquely by the following equation:

$$\frac{\delta_0}{\delta_{\max}} = \frac{r}{R_{M\max}}, \quad (8)$$

which coincides with the relation derived from Eqs. (1), (2) and (5), (6).

4. Modeling and method of calculation for the microlayer evaporation system

The effect of microlayer evaporation on bubble growth for the typical bubbles, which has features of real vapor growth rate and the averaged or typical characteristic factors such as microlayer thickness, growth rate of microlayer radius and duration of microlayer presence, is investigated here with the

correlations of microlayer characteristics shown in section 3 and the numerical calculation for the unsteady heat conduction model. The two-dimensional (2D) heat transfer calculation used for determining the initial microlayer thickness and surface superheat at bubble inception in the previous study [10] was developed.

The heat transfer rate through the microlayer from the heat transfer surface to the vapor bubble and the vapor generation from the microlayer with the heat conduction of the heat transfer plate are calculated under the following assumptions:

- 1) The characteristics and configurations of the initial microlayer thickness δ_0 , are fixed and are not dependent on the heat flux and superheat of the heat transfer surface.
- 2) No liquid flow occurs during evaporation, and evaporation of the microlayer occurs by heat conduction due to a thin microlayer and short duration.
- 3) The heat flux is assumed to be zero in the dryout area of the microlayer.
- 4) Bubbles are isolated with no interference from other bubbles.
- 5) The vapor volume is calculated under the assumption that the vapor bubble is spheroidal.
- 6) The superheated layer thickness δ_T , from the heat transfer surface increases in the liquid phase and remains constant after bubble inception.

Given the maximum radius of the microlayer R_{Mmax} in Eqs. (3), (5) and (7), t_{Bd} and δ_{max} were determined as characteristics of the microlayer configuration for water, and the distribution of the initial microlayer thickness δ_0 on the heat transfer surface and the duration of the microlayer Δt_{Me} , were then determined. Equations (3), (5) were altered to (4), (6) for the case of ethanol. The variation of the microlayer radius R_M could then be determined. Thus, R_{Mmax} and for an individual measured bubble enables the microlayer characteristics for numerical calculation to be determined.

The physical model and flow chart for the numerical calculation are shown in Figs. 11 and 12, respectively. The phenomenon was assumed to be axisymmetric; therefore, 2-D cylindrical coordinates were adopted. The model consists of a heat transfer plate, a microlayer and a superheated bulk liquid layer. A radius of 1.2 times the maximum microlayer radius R_{Mmax} was used as the calculation domain and a 2 mm thick heat transfer plate with the physical properties of quartz glass used in the experiment were adopted. Calculations confirmed that the domain of the microlayer radius was sufficiently large so as not to disturb microlayer evaporation. A constant heat flux q_1 at the bottom of the heat transfer plate was assigned, and q_2 and q_3 denote the heat fluxes at the areas of the bulk liquid phase area outside of the microlayer and at the microlayer, respectively. The outer boundaries of the heat transfer surface and the bulk liquid phase were under adiabatic conditions.

The heat transfer surface superheat at bubble inception ΔT_i was calculated in the process of determination of the initial microlayer thickness as shown in the former report [10]. Other conditions for the calculation are the maximum microlayer radius R_{Mmax} , and the heat flux at the plate bottom surface q_1 , and their experimentally measured values are given.

The basic equations and boundary conditions for the calculation are given by Eqs. (9)-(19). $T_w(t, r, z)$ denotes the temperature of the heat transfer plate. f , Q_{ML} , R_{dry} , $\delta(t, r)$, k_l , α , and h_i represent the bubble period from bubble inception to the next, total heat by microlayer evaporation transferred in a vapor bubble during the microlayer period Δt_{Me} , radius of the dryout area, microlayer thickness, thermal conductivity of the liquid, thermal diffusivity, and the interfacial heat transfer coefficient at the microlayer surface expressed by Eq. (13), respectively. σ , L , ρ_v and R denote the evaporation coefficient, latent heat of evaporation, vapor density and gas constant, respectively, in Eq. (13). Under these conditions, the unsteady heat conduction in the heat transfer surface was calculated using Eq. (9). Based on assumption 2), the heat flux from the heat transfer surface to the microlayer was determined by one-dimensional steady-state conduction (Eq. (12)). Evaporation is driven from the interface of the microlayer surface by surface superheat ΔT , so that the microlayer thickness is reduced from the initial value δ_0 , according to Eqs. (12) and (17). The interfacial heat transfer coefficient h_i , has little significant effect on the evaporation rate of the microlayer calculated under variation of the evaporation coefficient σ , between 0.3 and 1.0; therefore, its resistance was ignored in this range. The superheated layer developed in the bulk liquid phase from the heat transfer surface according to Eq. (15) as reported by Torigai et al. [11] and then remained at a constant thickness (Eq. (16)) after bubble inception. The thickness of the superheated layer was calculated to be about approximately 1 mm for water, which is in good agreement with that measured by Yamagata et al. [12]. The heat transfer plate and the test liquid are initially at saturation temperature and atmospheric pressure. The heat transfer rate from microlayer is expressed by Eq.(19). Thus, it is possible to clarify the effect of microlayer evaporation under periodic steady state conditions.

$$\frac{\partial T}{\partial t} = \alpha \left\{ \frac{1}{r} \frac{\partial}{\partial r} \left(r \frac{\partial T}{\partial r} \right) + \frac{\partial^2 T}{\partial z^2} \right\} \quad (9)$$

$$q_1 = const. \quad (10)$$

$$q_2 = \frac{k_l}{\delta_T} \{ T_w(t, r, 0) - T_{sat} \} \quad (11)$$

$$q_3 = \frac{T_w(t, r, 0) - T_{sat}}{\{ \delta(t, r) / k_l + 1 / h_i \}} \quad (12)$$

$$h_i = \frac{2\sigma}{2 - \sigma} \frac{L^2 \rho_v}{\sqrt{2\pi R T_{sat}^3}} \quad (13)$$

$$q_3 = 0 \quad (\text{dryout region}) \quad (14)$$

$$\delta_T = \sqrt{\pi \alpha t} \quad (15)$$

$$\delta_T = const. \quad (16)$$

$$\delta(t, r) = \delta_0(r) - \frac{\int_0^t q_3 dt}{\rho_l L}$$

(17)

$$\delta(t, r) = 0 \quad (\text{dryout region}) \quad (18)$$

$$Q_{\text{ML}} = \int_0^{R_{M\text{max}}} 2\pi r \int_0^{M_{Me}} \left[k\Delta T / \left(\delta_0 - \frac{\int_0^t q dt}{\rho_l L} \right) \right] dt dr \quad (19)$$

5. Results and discussion

5.1 Heat transfer characteristics of microlayer in evaporation system

As previously described [10], the configuration of initial microlayer thickness was uniquely specified independent of the heat flux from the bottom of the heat transfer surface in the experiment range. However, investigation of the effect of heat flux was required as a process of heat transfer during microlayer evaporation for elucidating its mechanism. Here, the numerical calculation was conducted with variation of only the heat flux from the bottom of the heat transfer surface under the same surface superheat at bubble inception ΔT_i , and the results are shown in Figs. 13 and 14. Figure 13 gives a comparison between the calculation results under a heat flux of 103 kW/m², as used in the experiment, and under the assumption of 50 kW/m² at the heating plate position of $z=0$, $r=0.07$ mm with intermittent bubble generation. The periodic steady state was achieved after 7.0 s for heat flux of 103 kW/m². The bubble period decreased with increasing heat flux under equal surface superheat at bubble inception, ΔT_i . Comparisons of the variation in vapor generated by microlayer evaporation are shown in Fig. 14. The effect of heat flux on the vapor volume generated from the microlayer was not significantly large and the difference was less than 10% when the heat flux was increased twofold. Therefore, the heat consumed by microlayer evaporation is mainly dependent on the unsteady release of stored heat in the heating plate before bubble generation, i.e., it is dependent upon the unsteady temperature change of the heating plate rather than heat flux given at the plate bottom.

The characteristics of the microlayer evaporation process from the temperature change in heating plate are shown for water in Figs. 15 and 16 under the condition of and heat flux of 103 kW/m² shown in Fig.13. Since the bubble cycle was approximately 48 ms, the thermal penetration depth δ_h was determined from Eq. (20) to be 0.67 mm where α_w is thermal diffusivity of water.

$$\delta_h = \sqrt{12\alpha_w t} \quad (20)$$

The change in the temperature distribution at the plate surface $z=0$ in a cycle at periodic steady state is shown in Fig. 15(a), and that in a relatively short period corresponding to the bubble growth process is shown in Fig. 15 (b). It is confirmed that the temperature of the heating surface decreased with microlayer evaporation and was a minimum at $t_B=13$ ms, and then recovered after bubble departure. Figure 16 shows the change in the temperature distribution at a penetration depth of $z=0.67$ mm corresponding to a bubble cycle. There was no significant effect of temperature variation at this position. Thus, it is confirmed that the enthalpy stored in the heating plate within the distance from the heating surface to the penetration depth during the interval of bubble suspension was consumed by microlayer evaporation through

unsteady thermal conduction due to the short period of the bubble cycle. Therefore, the heat flux from the bottom of the heating plate had a little effect on the microlayer evaporation rate and mainly determined the length of a bubble cycle as a time-averaged heat supply.

5.2 Effect of microlayer evaporation on bubble growth

The relation between the surface superheat at bubble inception and the heat transfer rate calculated by microlayer evaporation for water and ethanol is shown in Figs. 17(a) and (b), respectively, with maximum microlayer radius as a variable parameter. The heat transferred from microlayer evaporation for ethanol was approximately one third of that for water due to the lower thermal conductivity and thicker microlayer thickness of ethanol than water. The heat transfer rate increased with increasing surface superheat and maximum microlayer radius due to increases in the heat flux, area of heat transfer, and duration of microlayer evaporation for both liquids. Moreover, the total heat for microlayer evaporation increased linearly with surface superheat in outline form, but the increasing rate decreased in more closely manner. These trends are related to the appearance of dryout area that increases with increasing surface superheat, as discussed later.

Figures 18(a) and (b) show the relations between the maximum dryout radius and surface superheat at bubble inception with a parameter of maximum microlayer radius for water and ethanol, respectively. The dryout radius represents the radius of the dried area of the microlayer due to evaporation. The relations between the dryout radius and surface superheat at bubble inception are quantitatively similar in every bubble. The dryout radius increased with increasing superheat and was 0.2-1.0mm before bubble departure in this experimental range both for water and ethanol.

Variations in the ratio of vapor volume by microlayer evaporation to vapor volume of the entire bubble, V_{ML}/V_B , are shown in Figs. 19 (a) and (b) for water and ethanol, respectively. V_B was obtained from the images taken in the experiment and V_{ML} was calculated by microlayer evaporation. The vertical dotted lines indicate the commencement of bubble departure (decrease of microlayer radius). The ratio of the contribution of microlayer evaporation increased with bubble growth until the middle stage and then became almost constant.

The relations between the ratio of V_{ML}/V_B and the superheat of the heating surface at bubble inception are shown in Fig. 20(a) and (b) for water and ethanol. The value on the ordinate corresponds to the time at commencement of bubble detachment from the surface, as indicated by the dotted lines in Fig. 19. The results for both water and ethanol are similar. The ratios of V_{ML}/V_B were 15-70% in the range of $\Delta T_i = 6-39K$, and the ratio of V_{ML}/V_B increased linearly with the increase of surface superheat. V_{ML}/V_B had a little dependency on R_{Mmax} , and increased with decreasing R_{Mmax} . The relationship between V_{ML}/V_B and the surface superheat at bubble inception are expressed by least squares fitting in Eqs. (21) and (22) for water and ethanol, respectively.

$$\frac{V_{ML}}{V_B} = 1.89 \times 10^{-2} \times \Delta T_i \quad (21)$$

$$\frac{V_{ML}}{V_B} = 1.76 \times 10^{-2} \times \Delta T_i \quad (22)$$

Thus, the occupation ratios of vapor volume from microlayer evaporation to the vapor of the entire bubble for water and ethanol resemble each other. The evaporations from the microlayer and from the interface between the vapor in a bubble and superheated bulk liquid supply vapor into the bubble, and both phenomena are dominated mainly by heat conduction in the liquid layer. Hence, the appearance of similar values for water and ethanol could be understood. The surface superheat at bubble inception is varied widely under similar heating conditions as seen in Fig. 20, because there is little necessarily fixed relation among the heat flux of heating, surface superheat, and the temperature of superheated bulk liquid, due to the essential effects of other possible factors in boiling phenomena such as the bubble inception conditions due to surface heterogeneity and so forth.

5.3 Discussion on precision of results

An influence of precision of experimental results on simulation results is examined here. Generally speaking, since there are so many factors, which are not necessarily known clearly up to now, there are larger deviations in the measurement of boiling phenomena. Therefore, considering such features of boiling phenomena, we determined that the typical bubble behaviors were considered as described in Sec.4. That is, the averaged and typical bubbles, whose features defined as the variation of R_M/R_{Mmax} given in Fig.8 and the linear curves given in Figs.9 and 10 and selected them for analyzing the characteristics of boiling phenomena. The scatterings of the measured quantities shown in Figs.5-7 were reduced by the normalization as shown in Figs.8-10. Those quantities could be adopted as the characters of specific and typical bubbles. Also, the microlayer thickness shown in Eqs.(1) and (2) is reliable because the results were coincided with measurements of other researchers as shown in Fig.2 and 3.

As the result, after typical bubble characteristics was defined, the measured values given as conditions in the calculation were mainly q , R_{Mmax} and ΔT_i . The effect of change in q was little as described in the former study [10] and the measured R_{Mmax} and V_B were exact because of the reading from clear images with high resolution. Therefore, the major factor relating the error on V_{ML} , R_{dry} and V_{ML} / V_B was attributed to the measurement precision of ΔT_i . It is probable that there are two kinds of errors in ΔT_i ; one was measurement error due to the determination in the process of estimation of initial microlayer thickness [10]. Another was inevitable because of the essential non-uniformity in boiling phenomena such as nucleation characteristics, temperature fluctuation in superheated layer and so on. It is difficult to distinguish those effects in the measurement.

The effect of measurement errors in microlayer thickness, which was examined in the former report [10], was investigated here for water. The investigation of error in the microlayer thickness on the ΔT_i was shown in Fig.21(a) for the datum shown by red closed square in Fig.21(b) is located on the least square curve with little error. The original initial microlayer thickness δ_0 was decided by

numerical simulation iteratively with assuming ΔT_i by the curve fitting as seen solid line and circles in Fig.21(a). The symbols of triangle and square denote the values with adding the maximal errors of measurement ($\pm 1.7\mu\text{m}$) shown by dotted lines in Fig.21(b) [10] and similar process to determine δ_0 and ΔT_i was performed. As seen in Fig.21(a), the errors in ΔT_i were in the range within 5% when the maximal range of measurement error in microlayer thickness were adopted. For ethanol, the situation was similar to that for water. Thus, the measurement error of microlayer thickness had little effect on ΔT_i . As a result, it is probable that the major trend of the contribution of microlayer evaporation on the bubble growth in nucleate boiling shown in Fig.20 with widely ranged surface superheat were approved as the inherent feature of boiling phenomena due to its spatio-temporal non-uniformity.

6. Conclusions

During the process of pool nucleate boiling in an isolated bubble region for water and ethanol, heat transfer characteristics related to microlayer evaporation on the basis of the measured microlayer structure that forms underneath the vapor bubble under a heat flux of 50-103 kW/m² for water and 105-143 kW/m² for ethanol were investigated by using the normalization of measurement results of microlayer characteristics and 2-D heat transfer simulation. The results are summarized as follows.

- (1) The dominant factors that determine the microlayer characteristics, such as the microlayer thickness distribution, duration of the microlayer, and the size of the microlayer area on the heat transfer surface, were expressed in simple non-dimensional forms based on similarities in the bubble growth rate.
- (2) The basic characteristics concerning microlayer evaporation in the isolated bubble region of nucleate boiling was elucidated on the basis of the microlayer characteristics expressed in simple forms and numerical calculations from the modeling of nucleate boiling.
- (3) The effect of heat flux of heating was not significant under the condition of a quartz glass heating plate, and the heat consumed by microlayer evaporation was provided mainly from the unsteady temperature change of the heating plate.
- (4) The relationship between the ratio of vapor volume by microlayer evaporation to the vapor volume of an entire bubble, V_{ML}/V_B , and the surface superheat at bubble inception were investigated for water and ethanol to elucidate the contribution of microlayer evaporation. The ratios of V_{ML}/V_B were 15-70% in the range of surface superheat at bubble inception of 6-39 K. The ratio increased linearly with surface superheat at bubble inception.

Acknowledgments

The present study was supported in part by a Grant-in-Aid ((B)17360096) for Scientific Research from the Ministry of Education, Culture, Sports, Science and Technology of Japan.

References

- [1] F.D. Moore, R.B. Mesler, The measurement of rapid surface temperature fluctuations during nucleate boiling of water, *AIChE J.*, 7(4) (1961) 620–624.
- [2] M.G. Cooper, A.J.P. Lloyd, The microlayer in nucleate pool boiling, *Int. J. Heat Mass Transfer*, 12 (1969) 895–913.
- [3] T. Yabuki, O. Nakabeppu, On heat transfer mechanism of nucleate boiling with MEMS sensors (3rd Report, evaluation of the approach method and heat transfer characteristics of isolated boiling bubble), *Trans. Jpn. Soc. Mech. Eng. (Ser. B)* 76(771) (2010) 1932–1941.
- [4] R. Sharp, *The Nature of Liquid Film Evaporation during Nucleate Boiling*, NASA TN D-1997, Lewis Research Center, Cleveland, Ohio, 1964.
- [5] H.H. Jawurek, Simultaneous determination of microlayer geometry and bubble growth in nucleate boiling, *Int. J. Heat Mass Transfer*, 12 (1969) 843–848.
- [6] C.M. Voutsinos, R.L. Judd, Laser interferometric investigation of the microlayer evaporation phenomenon, *J. Heat Transfer*, 97(1) (1975) 88–92.
- [7] L.D. Koffman, M.S. Plesset, Experimental observations of the microlayer in vapor bubble growth on a heated solid, *Int. J. Heat Mass Transfer*, 5 (1983) 625–632.
- [8] M. Gao, L. Zhang, P. Cheng, X. Quan, An investigation of microlayer beneath nucleation bubble by laser interferometric method, *Int. J. Heat Mass Transfer*, 57 (2012) 183–189.
- [9] Y. Utaka, K. Nakamura, A. Sakurai, K. Itagaki, A. Sonoda, Configuration of microlayer in nucleate boiling, *Trans. Jpn. Soc. Mech. Eng. (Ser. B)*, 74(747) (2008) 2358–2364.
- [10] Y. Utaka, Y. Kashiwabara, M. Ozaki, Microlayer structure in nucleate boiling of water and ethanol at atmospheric pressure, *Int. J. Heat Mass Transfer*, 57 (2013) 222–230.
- [11] K. Torigai et al., Boiling heat transfer, *Jpn. Soc. Mech. Eng.* (1965).
- [12] K. Yamagata, F. Hirano, K. Nishikawa, H. Matsuoka, Nucleate boiling of water on the horizontal heating surface, *Memoirs of the Faculty of Engineering, Kyushu University*, 15–16 (1955) 97–163.

Figure Captions

- Fig.1 Schematic diagram of method for measurement of microlayer thickness
- Fig.2 Variation of initial microlayer thickness as a function of distance from incipient bubble site for water
- Fig.3 Variation of initial microlayer thickness as a function of distance from incipient bubble site for ethanol
- Fig.4 Definition of times relating to size of microlayer and bubble growth
- Fig.5 Variation of microlayer radius on heat transfer surface
- Fig.6 Variation of bubble departure time as a function of the maximum microlayer radius
- Fig.7 Variation of microlayer duration as a function of distance from the incipient bubble site
- Fig.8 Variability of dimensionless radius of microlayer over dimensionless time
- Fig.9 Variation of dimensionless microlayer duration as a function of dimensionless position
- Fig.10 Relation between dimensionless microlayer thickness and dimensionless position
- Fig.11 Model used for numerical calculation
- Fig.12 Flow diagram for the numerical calculation
- Fig.13 Heat transfer surface temperature as a function of time
- Fig.14 Volume of vapor from the microlayer as a function of time
- Fig.15 Variation of Distribution of heat transfer surface temperature under a in periodic steady state
- (a) Entire cycle
 - (b) Early stage in the cycle
- Fig.16 Distribution of heat transfer surface temperature as a function of time for water
- Fig.17 Variation of total heat through the microlayer as a function of surface superheat at bubble inception
- (a) Water
 - (b) Ethanol
- Fig.18 Variation of radius of dryout region as a function of surface superheat at bubble inception
- (a) Water
 - (b) Ethanol
- Fig.19 Contribution of evaporation from the microlayer as a function of normalized time
- (a) Water
 - (b) Ethanol
- Fig.20 Contribution of evaporation from the microlayer as a function of surface superheat at bubble inception
- (a) Water
 - (b) Ethanol
- Fig.21 Investigation of error in initial microlayer thickness on initial surface superheat of heat transfer plate

- (a) Determination of initial surface superheat in the process of deciding initial microlayer thickness
- (b) Distribution of initial microlayer thickness

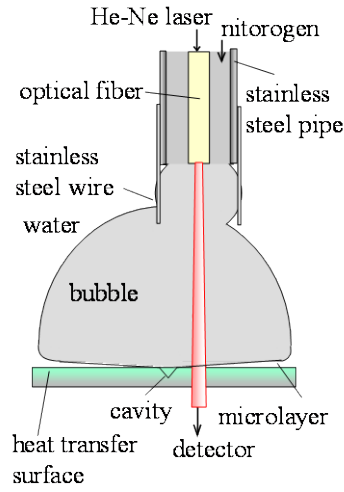


Fig. 1 Schematic diagram of method for measurement of microlayer thickness

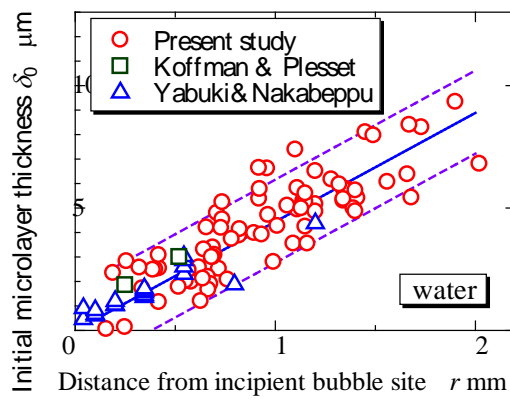


Fig. 2 Variation of initial microlayer thickness as a function of distance from incipient bubble site for water

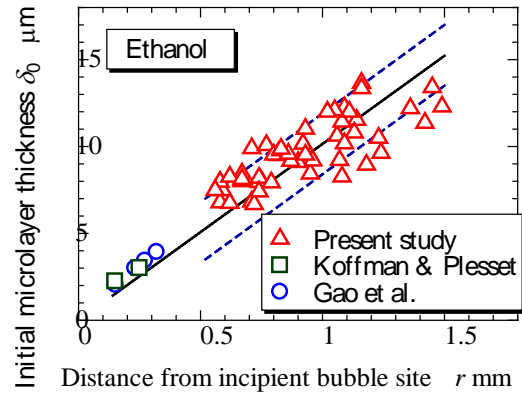


Fig. 3 Variation of initial microlayer thickness as a function of distance from incipient bubble site for ethanol

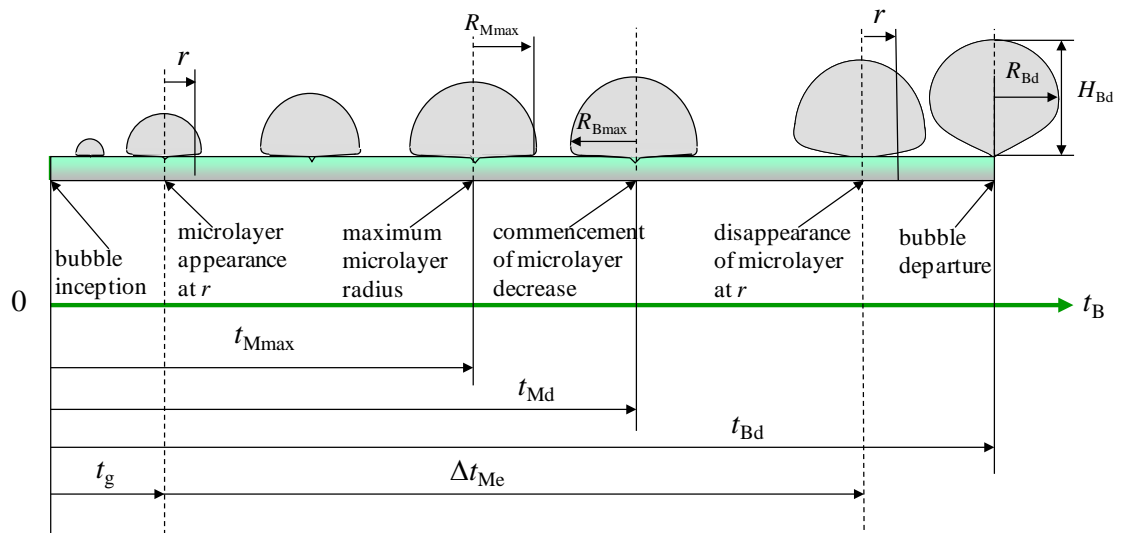


Fig. 4 Definition of times relating to size of microlayer and bubble growth

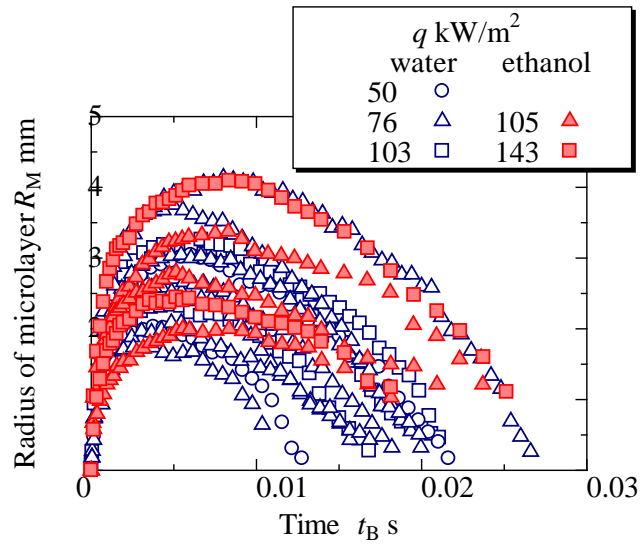


Fig. 5 Variation of microlayer radius on heat transfer surface

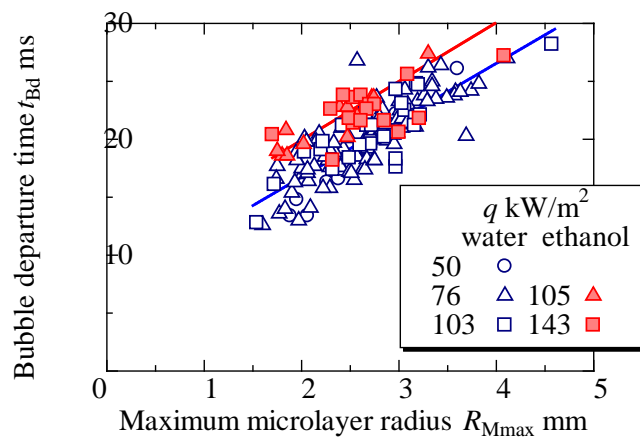


Fig. 6 Variation of bubble departure time as a function of the maximum microlayer radius

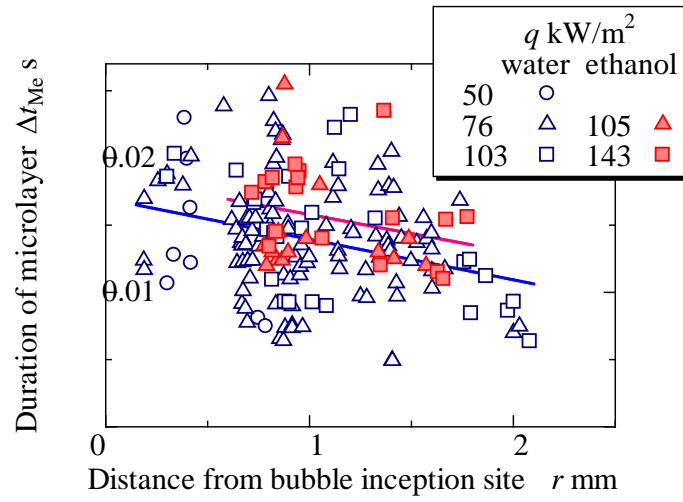


Fig. 7 Variation of microlayer duration as a function of distance from the incipient bubble site

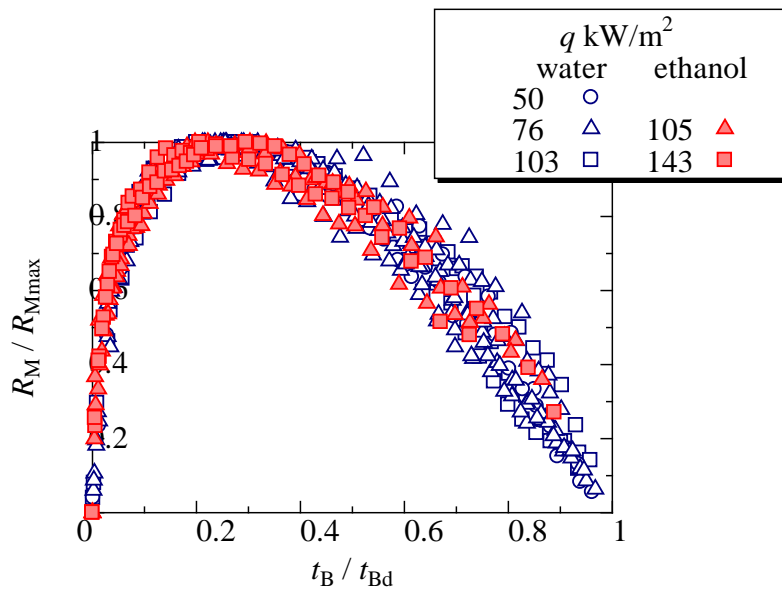


Fig. 8 Variation of dimensionless microlayer radius over dimensionless time

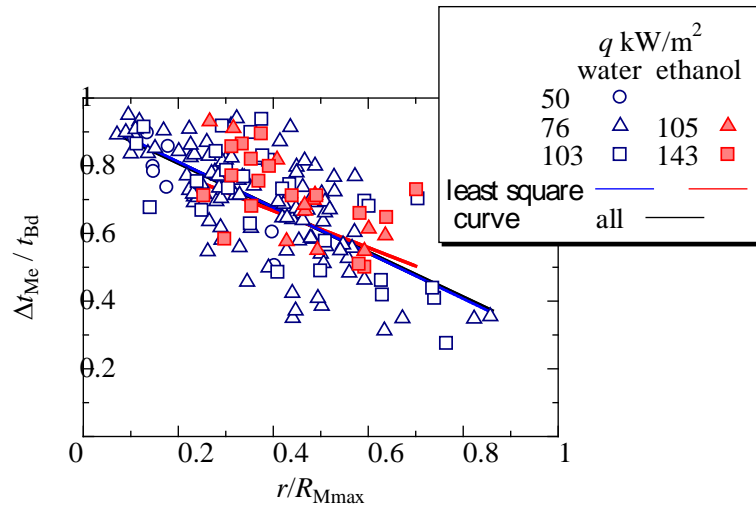


Fig. 9 Variation of dimensionless microlayer duration as a function of dimensionless position

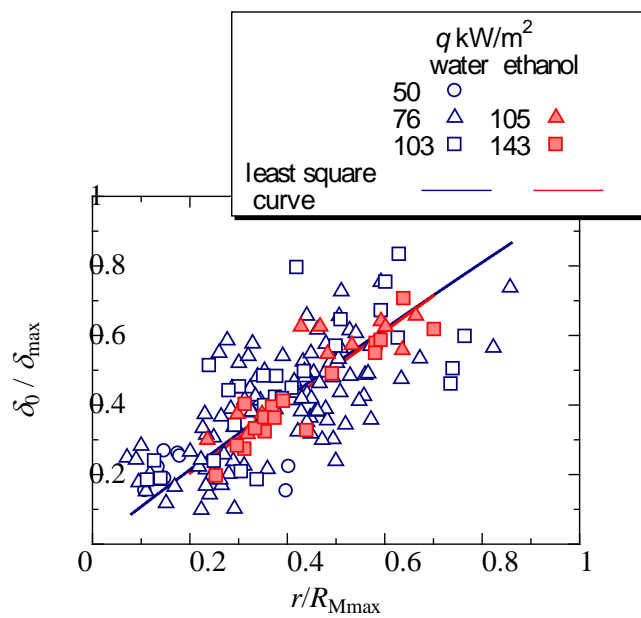


Fig. 10 Relationship between dimensionless microlayer thickness and dimensionless position

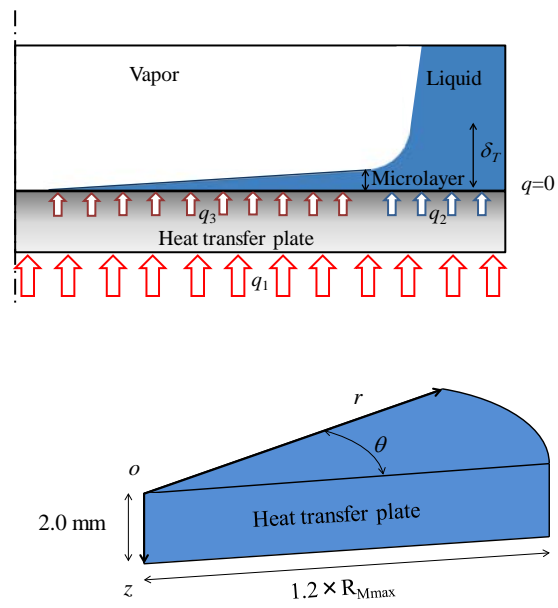


Fig. 11 Model used for numerical calculation

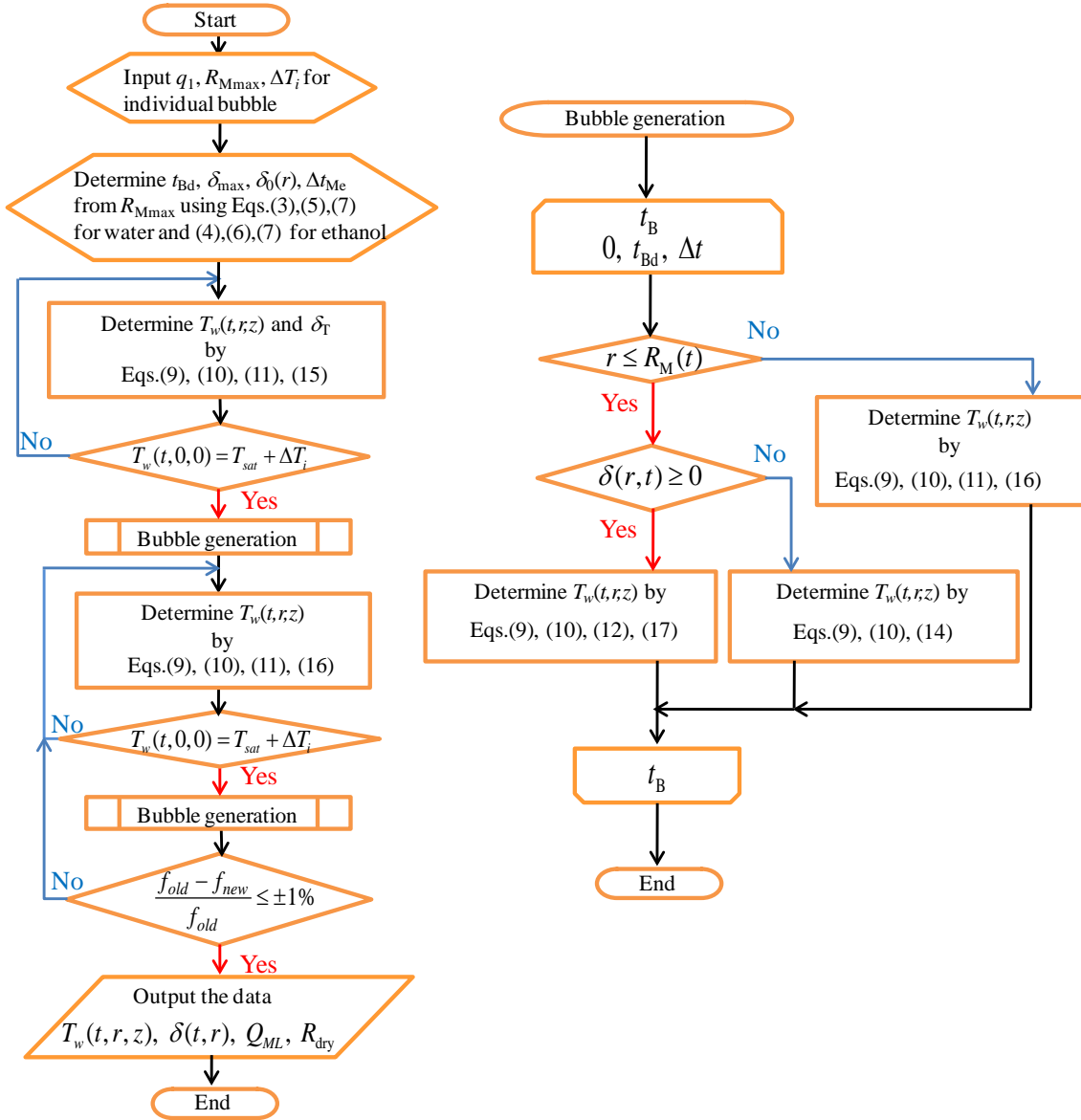


Fig. 12 Flow diagram for the numerical calculation

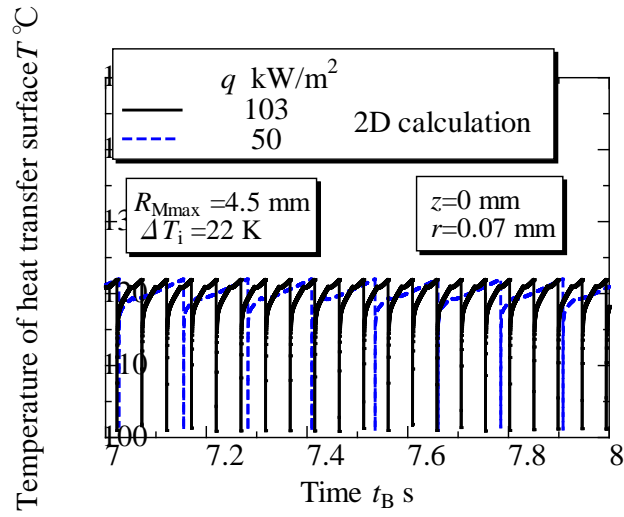


Fig. 13 Heat transfer surface temperature as a function of time

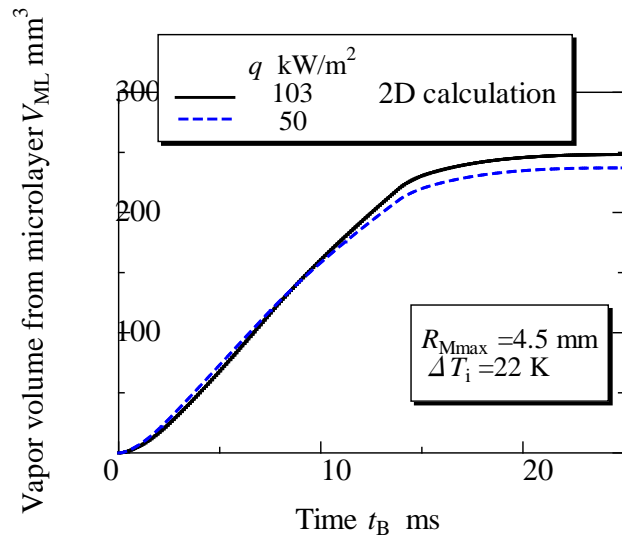
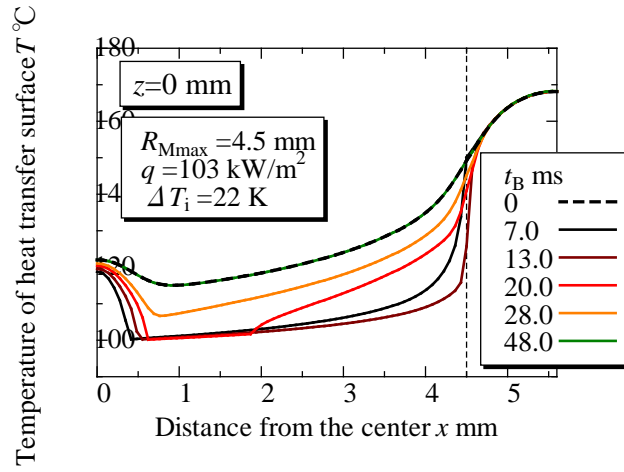
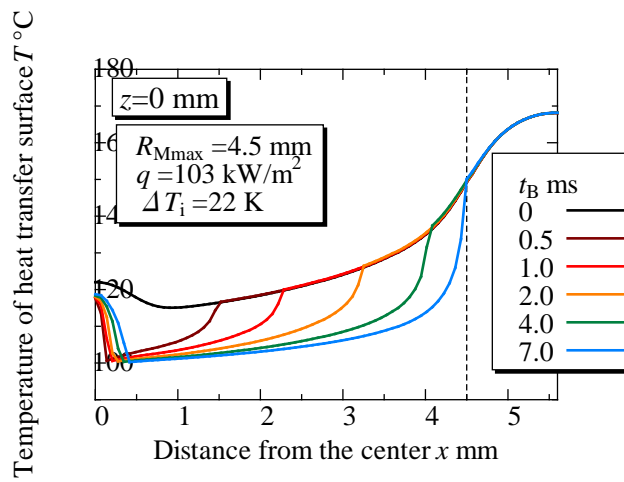


Fig. 14 Volume of vapor from the microlayer as a function of time



(a) Entire cycle



(b) Early stage in the cycle

Fig. 15 Variation of Distribution of heat transfer surface temperature under a periodic steady state for water

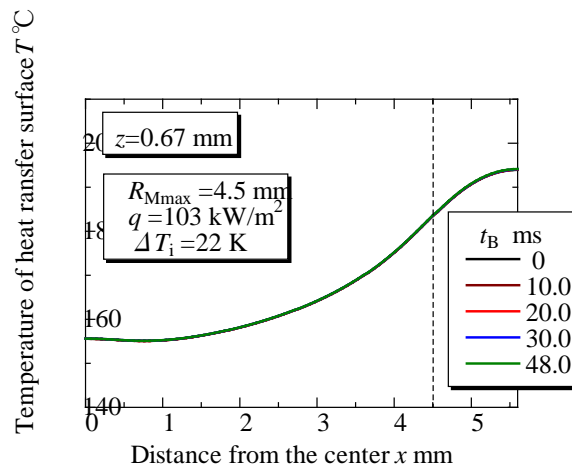
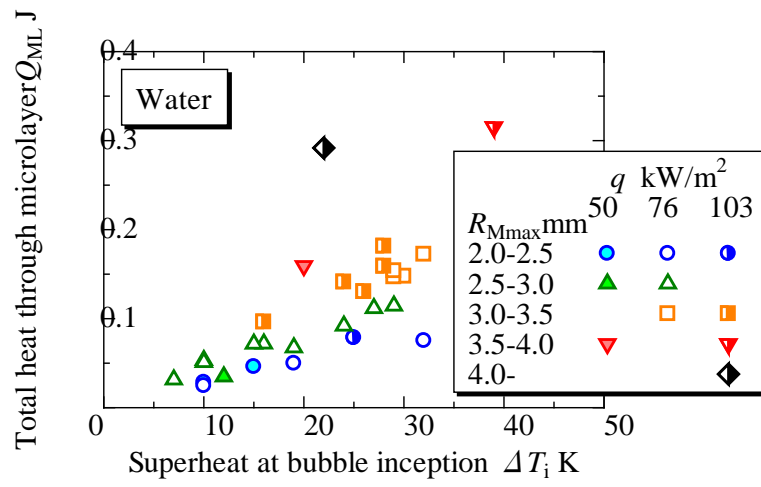
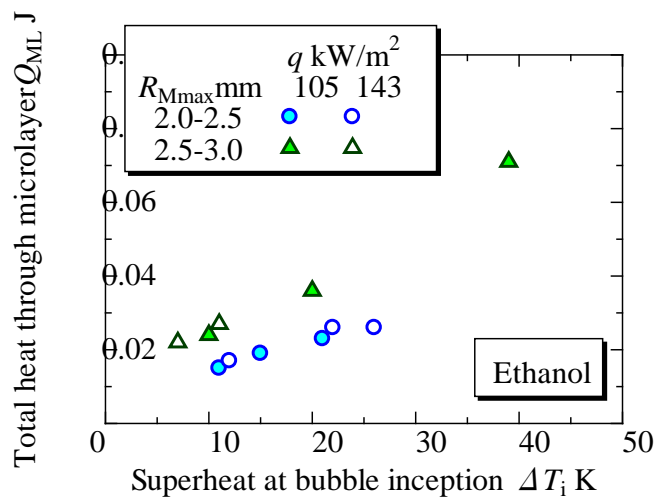


Fig. 16 Distribution of heat transfer surface temperature as a function of time for water

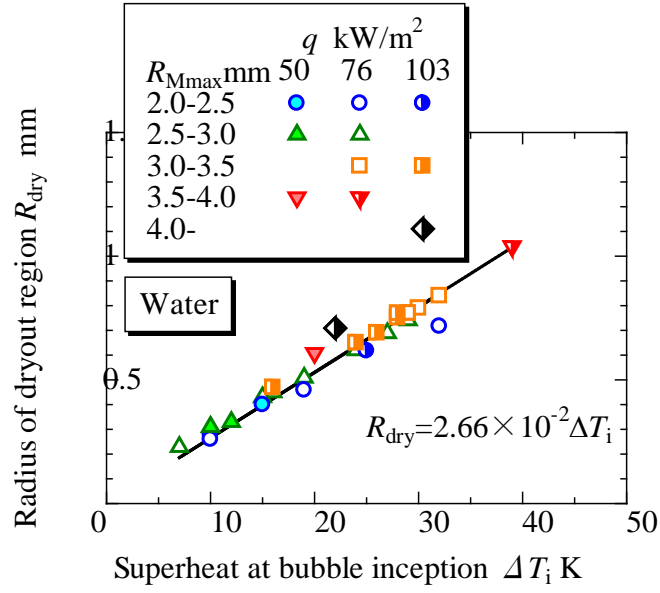


(a) Water

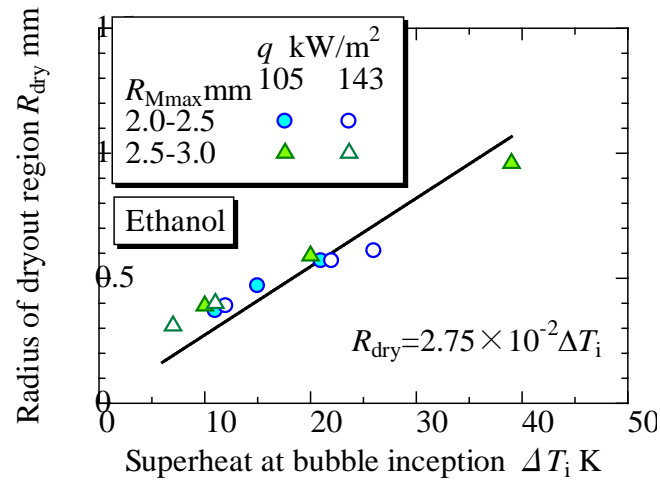


(b) Ethanol

Fig. 17 Variation of total heat through the microlayer as a function of surface superheat at bubble inception

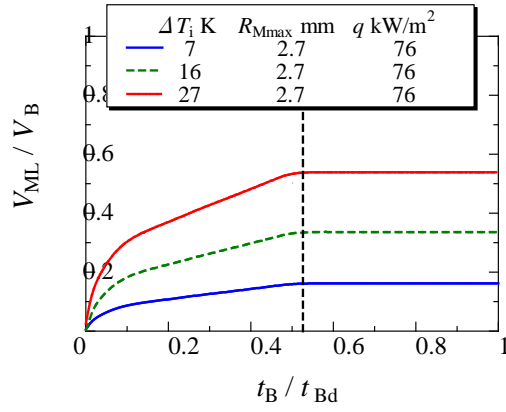


(a) Water

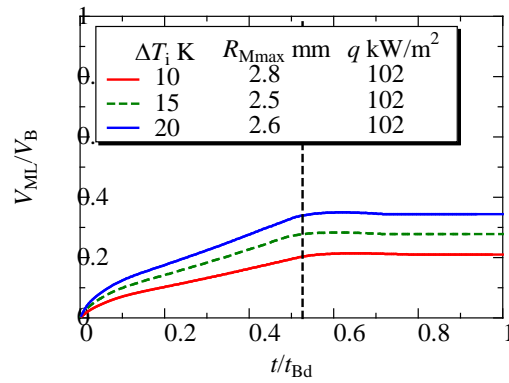


(b) Ethanol

Fig. 18 Variation of radius of dryout region as a function of surface superheat at bubble inception

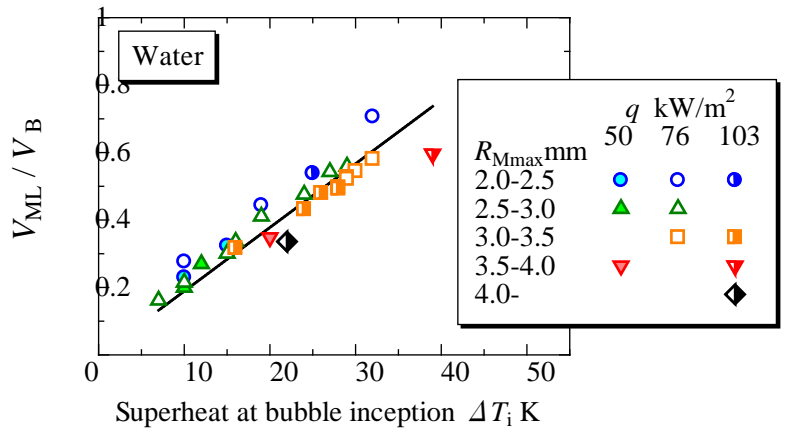


(a) Water

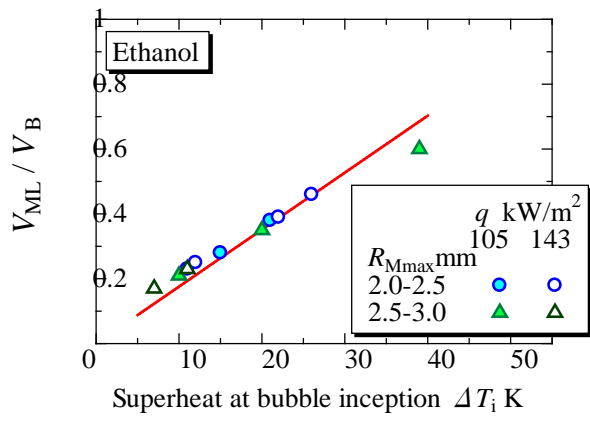


(b) Ethanol

Fig. 19 Contribution of evaporation from the microlayer as a function of normalized time

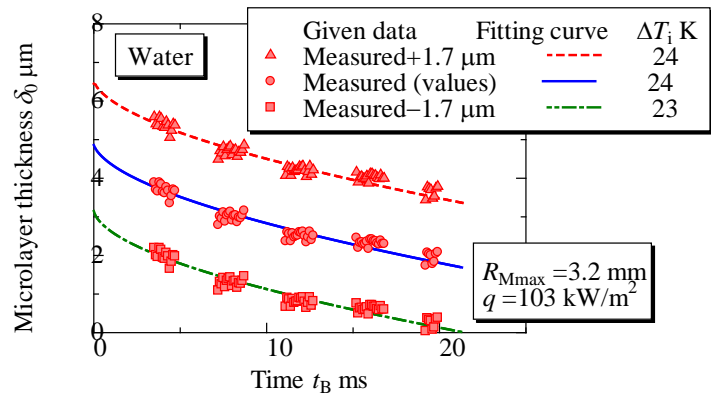


(a) Water

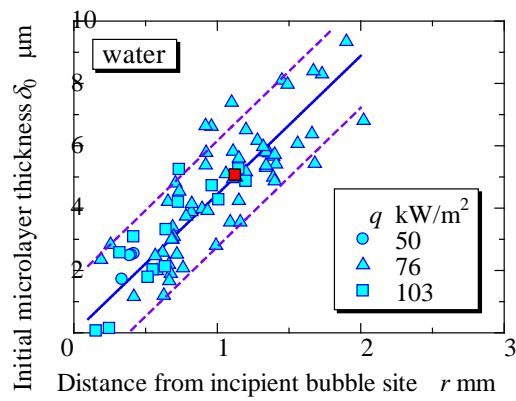


(b) Ethanol

Fig. 20 Contribution of evaporation from the microlayer as a function of surface superheat at bubble inception



(a) Determination of initial surface superheat in the process of deciding initial microlayer thickness



(b) Distribution of initial microlayer thickness

Fig.21 Investigation of error in initial microlayer thickness on initial surface superheat of heat transfer plate